Examination of diesel spray combustion in supercritical ambient fluid using large-eddy simulations

Wai Tong Chung[iD], Peter C Ma and Matthias Ihme[iD]

Abstract
High-pressure conditions in diesel engines can often surpass the thermodynamic critical limit of the working fluid. Consequently, the injection of fuel at these conditions can lead to complex behaviors that remain only incompletely understood. This study is concerned with investigating the application of a diffuse-interface method in conjunction with a finite-rate chemistry model in large-eddy simulations of diesel spray injection and ignition in a supercritical ambient environment. The presented numerical approach offers the capability of simulating these complex conditions without the need for parameter tuning that is commonly employed in spray-breakup models. Numerical simulations of inert and reacting *n*-dodecane sprays — under the Engine Combustion Network Spray A and Spray D configurations — are studied, and results are compared with experimental data for liquid/vapor penetration lengths and ignition timing. In addition, parametric studies are performed to identify flow sensitivities arising from the variation in nozzle diameters between both injectors, along with the impact of low-temperature oxidation on ignition in Spray D simulations. Spray A simulations are found to be insensitive to turbulence, and predictions for penetration length and ignition behavior are in good agreement with experiments. In contrast, Spray D predictions for penetration length and ignition delay demonstrated significant sensitivities to in-nozzle turbulence, introducing uncertainty to the predicted results and stipulating the need for quantitative measurements for model evaluation.

Introduction

Modern internal combustion engines typically operate under pressure and temperature conditions that exceed the thermodynamic critical limits of the in-cylinder gas. In diesel engines, the injection of liquid fuel at supercritical pressure and sub-critical temperature into a supercritical combustion chamber introduces complex thermo-physical phenomena that are currently not well understood.

Various experiments have been performed under Engine Combustion Network[1] (ECN) Spray A[2–8] and Spray D[9–18] target conditions in order to contribute to the understanding of diesel combustion. In addition, Reynolds-Averaged Navier–Stokes (RANS) and large-eddy simulations (LES) have been used to simulate Spray A[19–31] and Spray D[15,32–34] in computational investigations. Traditionally, Lagrangian particle methods that incorporate a two-phase model have been utilized assuming the presence of spray droplets.[15,23,25,28]

Although good agreement with experimental data have been reported, these methods often involve careful selection of the breakup and evaporation models along with parameter tuning.

By considering real-fluid thermodynamic and transport phenomena, Oefelein et al.[31] demonstrated that the injected liquid fuel in a diesel spray does not cross the liquid-vapor regime, enabling the effects of surface tension on mixing to be ignored. As a result, phenomena associated with traditional spray formation such as atomization, secondary breakup, droplet formation, and surface tension effects can be ignored.

Department of Mechanical Engineering, Stanford University, Stanford, CA, USA

Corresponding author:
Wai Tong Chung, Department of Mechanical Engineering, Stanford University, 488 Escondido Mall, Building 500, Stanford, CA 94305, USA.
Email: wtchung@stanford.edu

The presence of surface tension effects in diesel sprays under transcritical conditions remains a subject of active research. The term "transcritical" used in this article refers to the co-existence of sub-critical and supercritical (with respect to temperature) states. Using high-speed high-resolution microscopic visualization, Crua et al.[4] provided experimental evidence of surface tension for *n*-dodecane droplets under typical diesel engines conditions. Poursadegh et al.[6] examined the microscopic phase boundary of conventional liquid fuels under typical diesel conditions and found that the local Knudsen number exceeded the threshold for transition to a supercritical state, indicating the sub-critical nature of these fuels in diesel sprays.

By combining theoretical and experimental analyses, Poursadegh et al.[5] showed that, under certain conditions, the formation time of *n*-dodecane droplets exceeds the droplet vaporization time—allowing the atomization phenomena to be suppressed, and spray behavior to be controlled by single-phase mixing. These conditions could be described by diffuse-interface methods which treat fluid properties between liquid and gaseous regimes as a smooth function.

Yue and Reitz[24] combined LES with an Eulerian spray model that used similar time-scale arguments, and ignored droplet breakup, to simulate Spray A with good accuracy. Garcia-Oliver et al.[33] combined an Eulerian single liquid approach with a RANS framework to simulate Spray A under ambient and injector pressure, with more accurate predictions at higher injection and ambient pressures—highlighting the mixing-controlled hypothesis at typical diesel conditions.

Using a quasi-conservative model and entropy-stable algorithm,[35] Ma et al.[19] combined the diffuse-interface method with a compressible LES solver that also incorporated real-fluid effects and finite-rate chemistry, in order to simulate transcritical diesel spray combustion under Spray A conditions. Simulation results for penetration length and ignition delay were in good agreement with experimental data. In these simulations, the internal nozzle flow was not considered, and nozzle exit conditions were prescribed as a plug flow profile without any turbulent fluctuations, with time-dependent mass-flow rate calculated by the CMT virtual injection rate generator.[12] Matheis and Hickel[22] used a similar approach without introducing any turbulence by arguing that the jet breakup process is expected to be controlled by the strong shear forces induced by the high-speed jet.

The ECN Spray D configuration operates under the same ambient conditions as Spray A, but involves an injector with a nominal nozzle diameter that is twice the size of that in Spray A—which causes the Reynolds number *Re*, based on nozzle diameter, of Spray D to increase to approximately *Re* = 60,000. In addition, the *L/D* (length-to-diameter) ratio of Spray D is approximately half that of Spray A—at 5.4 and 11.2, respectively.[17] In an experiment involving the injection of liquid jets into a quiescent environment, Wu et al.[36] showed that injectors with passage *L/D* ratio exceeding 4 and nozzle diameter Reynolds number exceeding 40,000 can result in turbulent spray breakup. This suggests that Spray A and Spray D can possess reasonably different near-nozzle spray behavior.

As a consequence, neglecting effects of inlet turbulence and other in-nozzle phenomena may not be adequate when simulating Spray D. In addition, experimentalists have been using the ECN Spray D, alongside ECN Spray C, in order to investigate effects of in-nozzle cavitation on spray behavior.[9,11] As a result, simulations of Spray D typically require meshes that incorporate effects of nozzle geometry. High-resolution X-ray tomography by Matusik et al.[17] on Spray D injector nozzles has enabled the development of a high-resolution three-dimensional (3D) mesh for Spray D that can be incorporated in these simulations. Battistoni et al.[16] have presented LES and direct numerical simulation (DNS) of sub-critical inert Spray D injection using 2.5 and 1 μm cells, with fully resolved nozzle geometry. Westlye et al.[9] have combined a diffuse-interface method with LES to study the different spray behaviors caused by discrepancies between Spray C and D nozzle geometries. However, incorporating such an approach in the present work, where finite-rate chemistry and real-fluid effects are considered, presents a computational challenge.

The objective of this article is to perform LES with the diffuse-interface method and real-fluid thermodynamics to investigate *n*-dodecane sprays under Spray D conditions and compare results with Spray A calculations, under inert and reacting conditions, in order to identify the significance of in-nozzle phenomena in transcritical auto-ignition.

The remainder of this article is as follows: the next section discusses the method used to perform the spray LES. Then, the cases investigated under inert and reacting conditions, along with the computational setup employed, are described. Simulation results for Spray A and Spray D are then discussed and compared with experimental measurements,[2,9,11] before the conclusions are presented.

Method

The governing equations that are solved in the present study are the Favre-filtered conservation equations for mass, momentum, energy, and chemical species

$$\partial_t \bar{\rho} + \nabla \cdot (\bar{\rho}\tilde{u}) = 0 \tag{1}$$

$$\partial_t (\bar{\rho}\tilde{u}) + \nabla \cdot (\bar{\rho}\tilde{u}\tilde{u}) = -\nabla \cdot (\bar{p}\boldsymbol{I}) + \nabla \cdot (\bar{\boldsymbol{\tau}}_v + \bar{\boldsymbol{\tau}}_{SGS}) \tag{2}$$

$$\partial_t (\bar{\rho}\tilde{e}) + \nabla \cdot [\tilde{u}(\bar{\rho}\tilde{e} + \bar{p})] = \nabla \cdot [(\bar{\boldsymbol{\tau}}_v + \bar{\boldsymbol{\tau}}_{SGS}) \cdot \tilde{u}]$$
$$-\nabla \cdot (\bar{\boldsymbol{q}}_v + \bar{\boldsymbol{q}}_{SGS}) \tag{3}$$

$$\partial_t (\bar{\rho}\widetilde{Y}_k) + \nabla \cdot (\bar{\rho}\tilde{u}\widetilde{Y}_k) = -\nabla \cdot (\bar{\boldsymbol{J}}_{k,v} + \bar{\boldsymbol{J}}_{k,SGS}) + \bar{\bar{\boldsymbol{\omega}}}_k \tag{4}$$

with density ρ, velocity vector $\boldsymbol{u}$, pressure p, specific total energy e, stress tensor $\boldsymbol{\tau}$, and heat flux $\boldsymbol{q}$. Y_k, $\boldsymbol{J}_k$, and $\dot{\boldsymbol{\omega}}_k$ are the mass fraction, diffusion flux, and chemical source term for species k, respectively. Subscripts v and SGS denote viscous and turbulent quantities, respectively.

The system is closed using the Peng–Robinson cubic state equation in order to model real-fluid thermodynamics under transcritical conditions

$$p = \frac{RT}{v-b} - \frac{a}{v^2 + 2bv - b^2} \qquad (5)$$

with mixture-specific gas constant R and specific volume v. The coefficients a and b account for effects of intermolecular forces and volumetric displacement and are dependent on mixture temperature and composition.[37] The evaluation of internal energy, specific heat capacity, and partial enthalpy using the Peng–Robinson state equation has been described in detail in Ma et al.[21,35]

The dynamic viscosity and thermal conductivity are evaluated using Chung's method with high-pressure correction,[38] and Takahashi's high-pressure correction[39] is used to evaluate the binary diffusion coefficients.

In this study, a reduced 33-species mechanism that is derived from Yao et al.[40] is employed. Of the 54 species from the parent mechanism, 21 species are identified to be suitable for a quasi-steady state assumption—through zero-dimensional auto-ignition computations at $p = 60$ bar, and initial temperatures ranging from 800 to 1000 K. The reduced mechanism is incorporated into the computational fluid dynamics (CFD) solver using a Cantera library interface.[41] A more detailed explanation on the employed mechanism is provided by Ihme et al.[20]

To conduct these simulations, the unstructured compressible finite-volume solver Charles^x has been employed. In this solver, the convective fluxes are discretized using a sensor-based hybrid scheme[42] in which a high-order, non-dissipative scheme is combined with a low-order scheme to describe interfaces and flow-field discontinuities. Due to the density gradients present at trans- and supercritical conditions, an entropy-stable flux correction technique[35] is used to ensure the physical realizability of the numerical solution and to dampen non-linear instabilities in the numerical scheme. An adaptive double-flux method[35,43] is applied to eliminate spurious pressure oscillations. In this method, a second-order Strang-splitting scheme is employed to separate the non-stiff convection and diffusion operators from the reaction operator. A strong stability preserving third-order Runge–Kutta (SSP-RK3) scheme is used for time integration of non-stiff operators. The reaction chemistry is integrated using a semi-implicit Rosenbrock–Krylov scheme,[44,45] which is fourth-order accurate in time and has linear cost with respect to the number of species. The turbulent stresses are modeled using a Vreman[46] sub-grid scale (SGS) model, while turbulence/chemistry interaction is accounted for using the dynamic thickened-flame model[47] in which the maximum thickening factor is set to a value of 4 in this study.

Case description and computational setup

In the present study, the ECN[1] Spray A and Spray D configurations are simulated. A summary of the cases explored in this study is presented in Table 1. Both inert and reacting cases are considered. The effects of nozzle turbulence with turbulence intensities u'/U_{in} ranging from 0% to 5% are investigated for both spray configurations under inert conditions at $p_\infty = 6$ MPa, $T_\infty = 900$ K, with nitrogen used as the ambient gas. In addition, effects of inlet velocity profile on spray dynamics are examined using plug flow, parabolic, and power flow velocity profile.

Simulation for reacting Spray A is performed for $p_\infty = 6$ MPa, $T_\infty = 900$ K, 15% O_2. To consider effects of turbulence on nozzle exit conditions, two Spray D cases under reacting conditions with $u'/U_{in} = 0$% and $u'/U_{in} = 2$%, at $p_\infty = 9.34$ MPa, $T_\infty = 900$ K, and 20.9% O_2 are simulated to match experiments performed by Payri et al.[11] In addition, a Spray D case at $p_\infty = 6$ MPa, $T_\infty = 1200$ K, and 15% O_2, based on experiments by Westlye et al.,[9] is simulated. These cases were chosen for the high ambient pressure and temperature that result in shorter ignition delay, which reduces the computational cost of simulating spray auto-ignition.

As shown in Figure 1, a 3D cylindrical domain, discretized by a structured mesh with hexahedral elements,

Table 1. Summary of LES cases.

Case	Spray A	Spray D
T_∞ (K)	900	900 (1200, 900)
p_∞ (MPa)	6.00	6.00 (6.00, 9.34)
O_2 by mole	0.0% (15.0%)	0.0% (15.0%, 20.9%)
p_{rail} (MPa)	150	150
Nozzle diameter (μm)	90	186
u'/U_{in}	0%, 2%, 5%	0%, 2%, 5%

Values in parentheses denote conditions for the reacting cases.
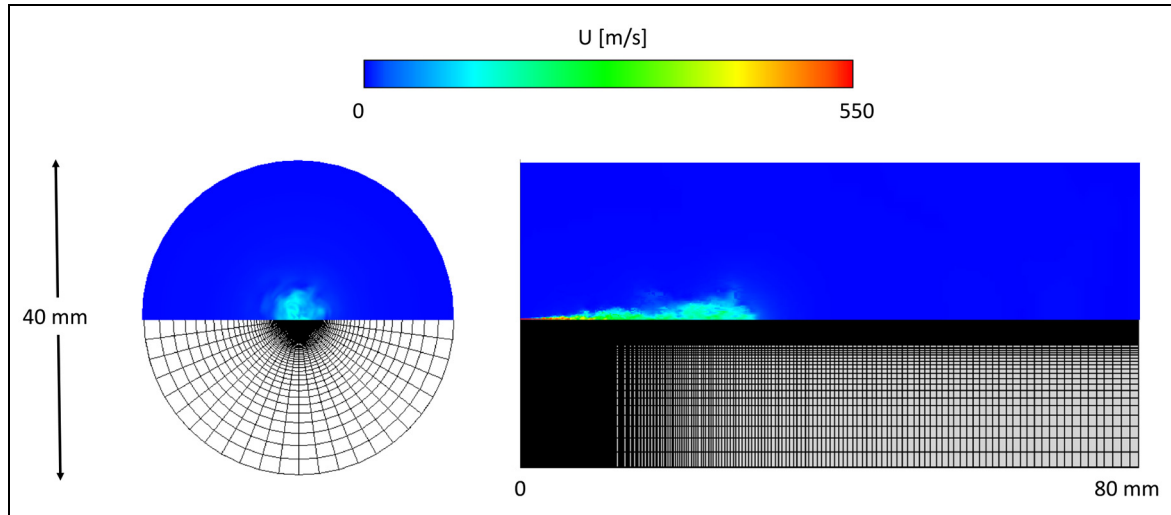
Figure 1. Radial (left) and axial (right) view of mesh used, along with velocity magnitude profiles. The mesh consists of 2.7 million grid points. Minimum cell size is 8 μm.

with a diameter of 40 mm and length of 80 mm is used in this study. The domain has been discretized into a total of 2.7 million grid points. A minimum grid spacing of 8 μm is selected in order to resolve the ignition kernels, the size of which is estimated through one-dimensional unsteady flamelet calculations. This mesh resolution is much smaller than the 62.5 μm cell size recommended by Wehrfritz et al.[48] in their mesh resolution study of inert Spray A. The injector geometry is not included in the simulations. Instead, boundary conditions that match nozzle conditions are assigned at the domain inlet.

The fuel mass flux at the domain inlet is determined using the time-dependent rate of injection, as provided by the CMT virtual injection rate generator.[12] Nominal inlet conditions prescribed by ECN[1,2] are used for Spray A; the Spray D inlet condition is generated with recommendations from Westlye et al.[9] Homogeneous isotropic turbulence, generated using the digital filter approach of Klein et al.[49] at various turbulence intensities with integral length-scale equal to nozzle diameter, is added to the mean velocity profile in order to consider the effects of in-nozzle turbulence.

The solution is advanced in time using a typical time step of 1.2 ns, with a unity Courant–Friedrichs–Lewy (CFL) number. The simulations were performed using 1440 Intel Xeon (E5-2698 v3) processors, and 4 μs of physical time could be completed in about an hour wall clock time for the reacting case.

Results and discussion

Inert conditions

Figure 2 compares the spray penetration lengths for Spray A and D under nominal conditions ($p_\infty = 6.00$ MPa, $T_\infty = 900$ K, $u'/U_{in} = 0\%$). These simulation results are compared with experimental

measurements[2,9] that were determined via Schlieren and Mie imaging for vapor and liquid penetration lengths, respectively. In these simulations, the vapor penetration length for both configurations is defined as the furthest axial position where the mixture fraction Z exceeds 0.01. The mixture fraction is defined with respect to *n*-dodecane mass fraction $C_{12}H_{26}$

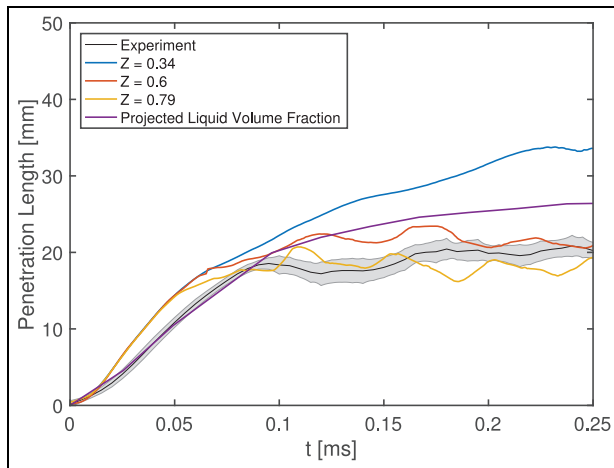$$Z = \frac{Y_{C_{12}H_{26}}}{Y_{C_{12}H_{26}} + Y_{N_2}} \quad (6)$$

A previous study[20] determined that the vapor penetration length did not change significantly for mixture fraction threshold values ranging from 0.1 to 0.01. Compared to Spray A, simulation for Spray D at $u'/U_{in} = 0\%$ slightly overpredicts the vapor penetration length between 0.1 and 0.7 ms. Liquid penetration predictions for both Spray A and Spray D are in good agreement with the experimental data, as can be seen in Figure 2.

A mixture fraction value of 0.6 is chosen to define the liquid region of Spray A and Spray D; this value provides the best agreement with the experimental data for the liquid penetration length in both sprays. A similar value was also employed by Oefelein et al.[31] in their real-fluid simulations. Unlike the threshold value for the vapor boundary, Figure 3 shows that the liquid penetration length is sensitive to the chosen mixture fraction value, showing significant differences in liquid penetration length predictions for mixture fractions ranging from 0.34 and 0.79; it should be noted that $Z = 0.34$ corresponds to the saturated vapor-liquid equilibrium mixture fraction, while $Z = 0.79$ has been noted as the mixture fraction with the most pronounced changes to liquid fuel density.[31] Figure 3 also compares the estimation of liquid penetration length with mixture fraction $Z = 0.6$ with the ECN-recommended approach, which bridges experimental and
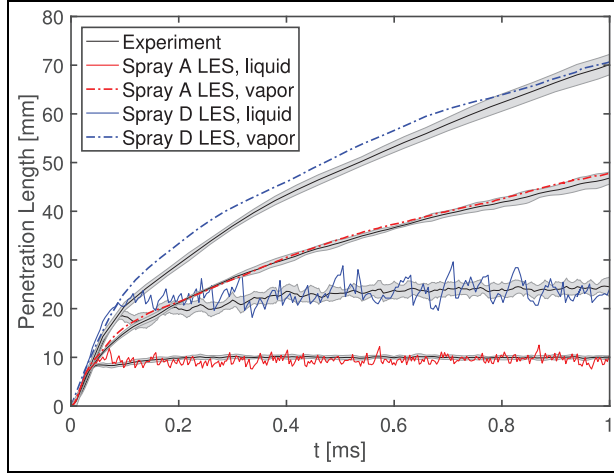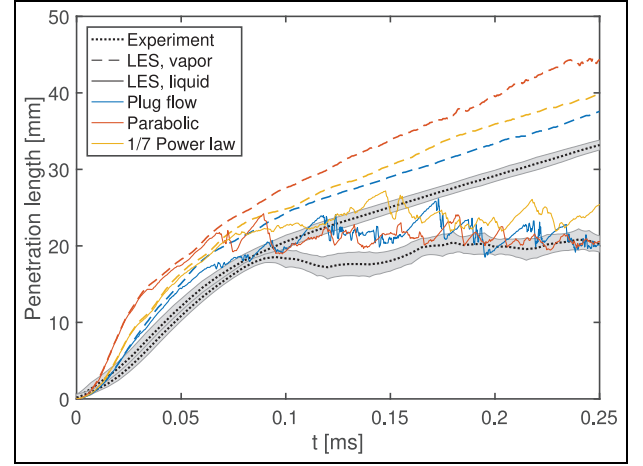
Figure 2. Comparison of liquid and vapor penetration length for Spray A and Spray D from simulation and experimental measurements[2,9] (inert, p_∞ = 6.00 MPa, T_∞ = 900 K, u'/U_{in} = 0%).

Figure 4. Spray D vapor and liquid penetration length predictions for different velocity profiles at the nozzle, with identical mass-flow rate, compared with experimental data[9] (inert, p_∞ = 6.00 MPa, T_∞ = 900 K, u'/U_{in} = 0%).

simulation results through calculating the liquid volume fraction projected on the cross-stream direction, $\int_{-\infty}^{\infty} \mathrm{LVF} dy$. Given the challenge in distinguishing liquid components in the absence of sharp interfaces, all cells with $Z > 0.34$ as "liquid droplets." Following ECN modeling standards, a set of $1\,\mathrm{mm}^3$ are placed on a cross-sectional plane, extracted from the simulation domain. The liquid volume fraction is then calculated by computing the volume fraction of the "liquid droplets" in each cube. $\int_{-\infty}^{\infty} \mathrm{LVF} dy$ is then computed using rectangular integration. The liquid penetration length is defined by the ECN as the furthest axial position where $\int_{-\infty}^{\infty} \mathrm{LVF} dy \geqslant 2 \times 10^{-3}\,\mathrm{mm}^3/\mathrm{mm}^2$. Reasonable agreement between both approaches is seen up to $0.15\,\mathrm{ms}$, with a slight deviation after that—likely caused by the fluctuating nature of the mixture fraction approach. Note that a moving average has been applied on Figure 3 to reduce the effect of these
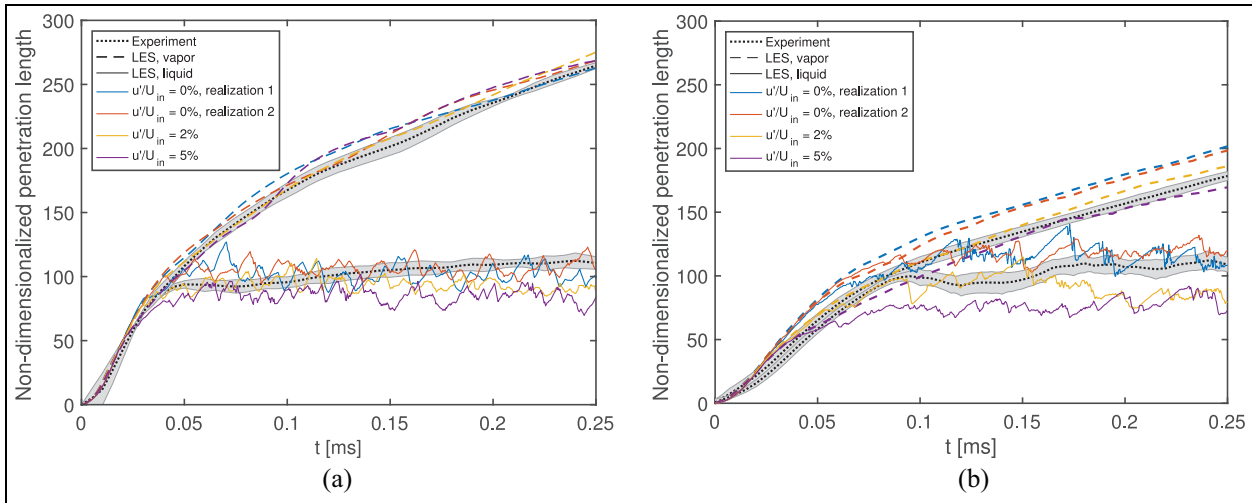
fluctuations, for better visual comparison between the different approaches.

Note that the fluctuations in the liquid penetration length in both Spray A and Spray D arise from the destabilization of the liquid core. During injection, the liquid core remains stable close to the nozzle due to large density gradients before small fragments of liquid at the tip break off from the core. These fragments continue to be transported downstream with large momentum that arise from the fragment's large density before transitioning into vapor phase. Fluctuations in Spray D are larger than fluctuations in Spray A due to the larger fragments, as a consequence of the larger liquid core.

Figure 4 demonstrates that the liquid and vapor penetration length calculations for Spray D are sensitive to the velocity profile prescribed at the inlet, despite identical mass-flow rates. Using a parabolic velocity profile results in the highest vapor penetration length prediction, while using a plug flow profile results in the lowest. This may be explained by the high centerline velocity in the parabolic profile and steeper velocity gradients in the shear layer, which in turns results in higher local momentum at the center of the jet. Similar effects of inlet velocity profile are seen at the initial stages of injection for the liquid penetration calculations. However, after the full development of the liquid jet at approximately $0.1\,\mathrm{ms}$, the liquid penetration length seems to be insensitive to the prescribed inlet velocity profile.

Figure 5(a) compares the vapor and liquid penetration lengths predicted by Spray A simulations[19] under different inflow turbulent intensities. For the cases without turbulence (u'/U_{in} = 0%), two realizations are conducted. It can be seen that the vapor penetration length for Spray A is insensitive to turbulent fluctuations introduced at the nozzle, as vapor penetration

Figure 3. Spray D averaged liquid penetration length evaluated using different evaluation criteria, compared with experiment[9] (inert, p_∞ = 6.0 MPa, T_∞ = 900 K, u'/U_{in} = 0%).

Figure 5. (a) Spray A and (b) Spray D vapor and liquid penetration length predictions for different turbulence intensities at the nozzle, compared with experimental data.[2,9] Note that penetration length has been non-dimensionalized with nozzle diameter for comparison (inert, $p_\infty = 6.00$ MPa, $T_\infty = 900$ K).
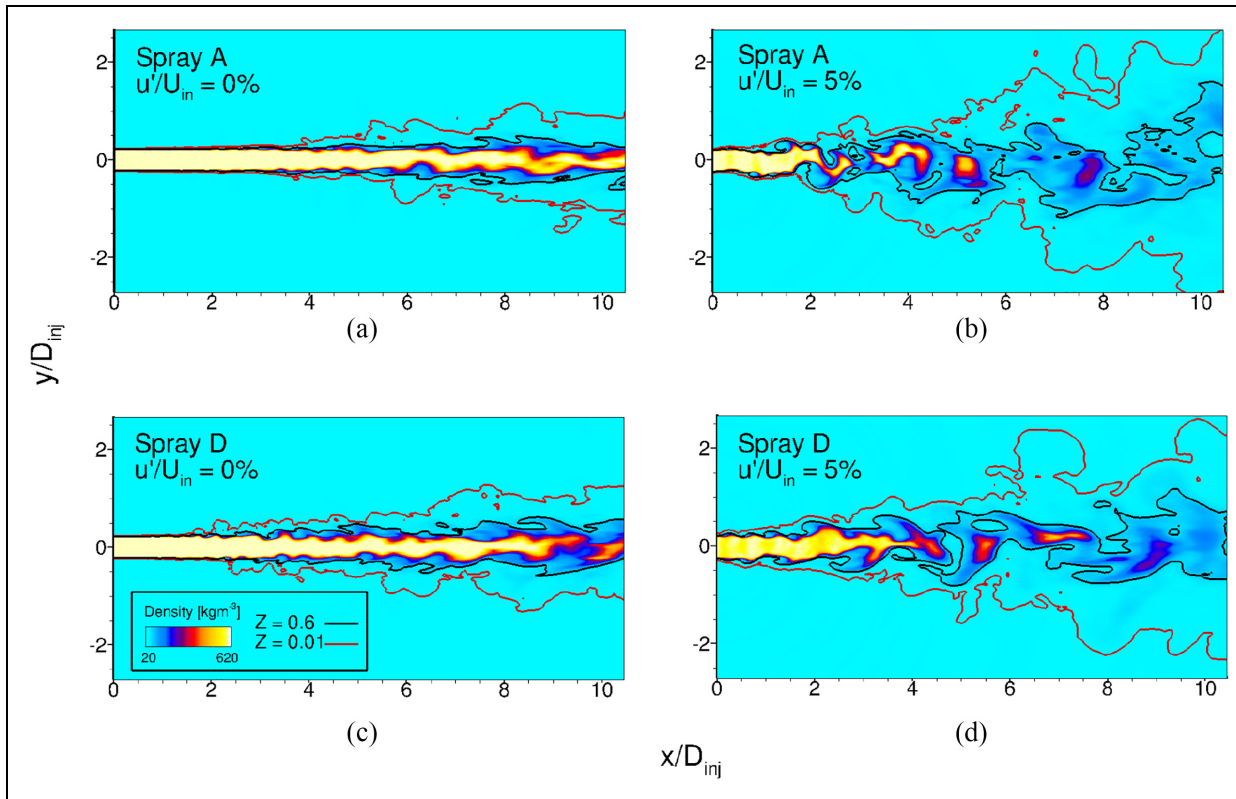
Figure 6. Density contours of (a) Spray A with u'/Uin=0%. (b) Spray A with u'/Uin=5%. (c) Spray D with u'/Uin=0%. (d) Spray D with u'/Uin=5% at steady-state liquid penetration. Note that contour dimensions are non-dimensionalized with nozzle diameter. Red lines mark the defined vapor threshold at $Z = 0.01$. Black lines mark the defined liquid threshold at $Z = 0.6$.

length for turbulence intensities of 2% and 5% remains similar to both realizations at 0%. However, the liquid penetration length for the simulations seems to be more sensitive to the nozzle turbulence; increasing turbulence intensity slightly decreases the liquid penetration length.

It should be noted that in supercritical jets, large density differences between the injected fluid and the ambient fluid can result in turbulence damping.[50] Figure 6(a) shows Spray A where $u'/U_{in} = 0\%$. The cylindrical liquid core near the nozzle remains unaffected by the surrounding flow in the simulated gas
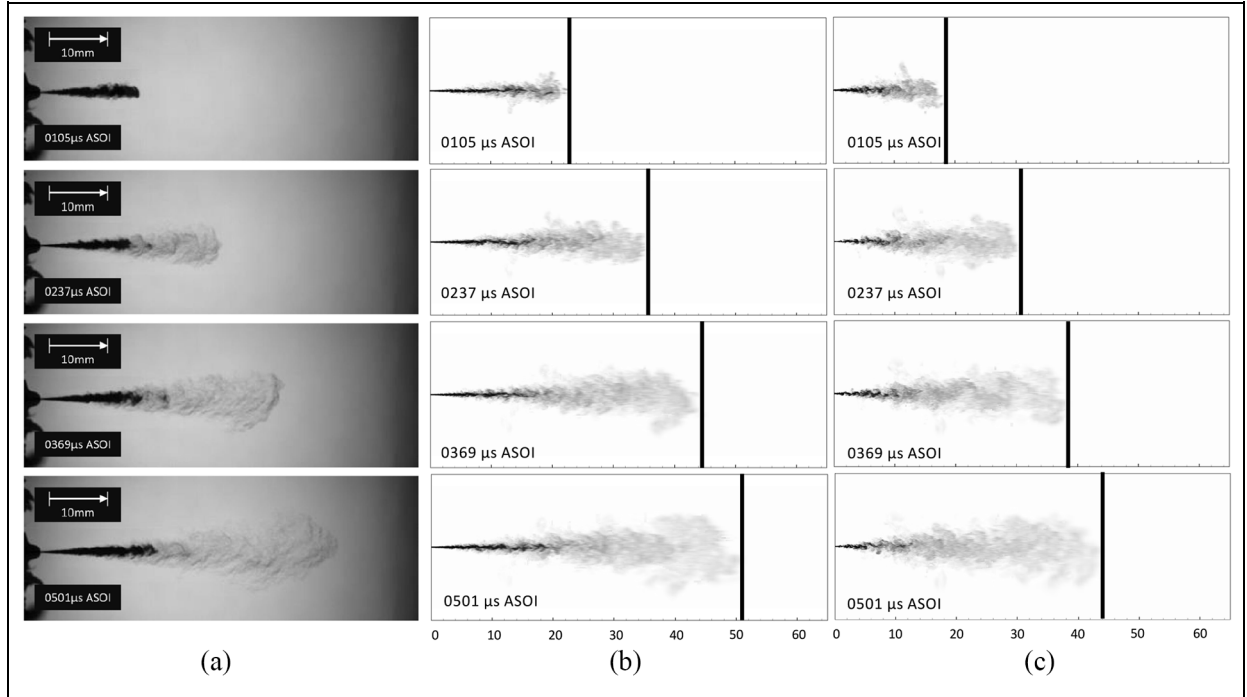
Figure 7. Time evolution of Spray D (inert, $p_\infty = 6.00$ MPa, $T_\infty = 900$ K). (a) Diffuse-back illumination images from an experiment.[11] (b) Mixture fraction contours from LES, $u'/U_{in} = 0\%$. (c) Mixture fraction contours from LES, $u'/U_{in} = 5\%$. Black lines are used to indicate spray penetration length.

chamber. However, as the spray develops, the liquid core, which is marked by black lines in Figure 6, increases in temperature from 363 to 900 K, reducing its density. This results in an increased spray angle, which is indicative of increased mixing and entraining of surrounding fluid into the jet core.

The consideration of 5% nozzle turbulence on Spray A can be observed in Figure 6(b). Turbulence promotes heat transfer between the cold injected fluid and hot ambient nitrogen. Thus, the liquid penetration length decreases slightly in Spray A at increasing nozzle turbulence intensities. The vapor penetration length in Spray A remains unaffected by nozzle turbulence for two reasons: (a) vapor regions of the injected fluid, marked within the red line in Figure 6, appear to have similar densities with the ambient nitrogen in both 0% and 5% nozzle turbulence intensities, hence effects of ambient flow on both cases remain similarly dominant and (b) the effects of nozzle turbulence on the liquid region are not significant enough to affect the evolution of the vapor region in Spray A. This is contrary to the simulation results for Spray D, as discussed below.

Figure 5(b) demonstrates the effect of various nozzle turbulence intensities on the Spray D vapor and liquid penetration length. Both liquid and vapor penetration lengths show appreciable sensitivity to inlet turbulence, especially in comparison with Spray A results in Figures 5(a), even at the same turbulence intensities. It can be seen that $u'/U_{in} = 2\%$ produces the best agreement with experimental results for both liquid and vapor penetration. The larger nozzle diameter in Spray D increases the jet Reynolds number. This causes faster turbulence breakup in Spray D than in Spray A. Adding turbulent fluctuations at the nozzle results in even faster breakup that is significant enough to affect the development of the entire spray, resulting in a reduction in vapor penetration lengths at greater nozzle turbulence intensities.

Figure 7 compares center-plane mixture fraction contours from Spray D where $u'/U_{in} = 0\%$ and $u'/U_{in} = 5\%$ with diffuse-back illumination images from experiments by Payri et al.[11] At 0% inlet turbulence, seen in Figure 7(b), the predicted liquid spray matches in length with the experimental images, as shown in Figure 7(a). Consideration of 5% inlet turbulence, seen in Figure 7(c), reduces the liquid portion nearly by a factor of 2; the liquid spray is also visibly perturbed by turbulence. At 503 μs, the vapor penetration length is about 10 mm shorter than that for the case with 0% turbulence. The spray angle widens with the introduction of nozzle turbulence.

Reacting condition

Table 2 compares ignition delay predictions for Spray A and Spray D with experimental results by Lillo et al.,[2] for Spray A, and Westlye et al.[9] and Payri et al.,[11] for Spray D. Ignition delay data by Lillo et al. and Westlye et al. were determined through OH* chemiluminescence imaging with a 50% threshold, while Payri et al. evaluated ignition delay with the rate of change of density gradients using Schlieren imaging; a

Table 2. Comparison of ignition delay τ_{ig} predictions for Spray A and Spray D with experimental data.[1,9,11]

| Case	T_∞ (K)	p_∞ (MPa)	%O_2	u'/U_{in} (%)	τ_{ig}^{exp} (μs)	τ_{ig}^{LES} (μs)
Spray A	900	6.00	15.0	0	409 ± 10	352
Spray D	1200	6.00	15.0	0	147	149
Spray D	900	9.34	20.9	0	238	146
Spray D	900	9.34	20.9	2	238	167

good agreement between both experimental methods was reported.[11] LES ignition delay is determined by observing the time taken to reach 14% of the maximum OH mass fraction; this value was found to be in good agreement with the 50% OH* chemiluminescence threshold for experimental measurements.[26]

In comparison with experimental data, the LES under-predicts Spray A ignition delay by approximately 10%. A similar deviation was also reported by Yao et al.[40]—from whom the present chemical mechanism is adapted—with the discrepancy credited to a simplified low-temperature oxidation sub-mechanism. This under-prediction is also seen in simulations of Spray D at 900 K ambient temperature, under-predicting auto-ignition by approximately 35%. In addition to the deviation caused by low-temperature oxidation, the ambient pressure of 9.34 MPa, which is a parametric variation of the recommended 6 MPa, may introduce variations to Spray D ignition behavior. Yao et al.[40] showed that Spray A simulation conducted at 4 MPa and 900 K ambient pressure and temperature can result in approximately 40% error in ignition delay prediction. To examine the impact of different ambient pressure and temperature, we conducted LES calculations for Spray D at 6 MPa and 1200 K. These results showed

significant improvements in ignition delay prediction, with 2% error, due to the dominance of high-temperature oxidation in characterizing ignition behavior.

An additional source of uncertainty in ignition behavior of the Spray D simulations is the sensitivity of the spray to in-nozzle conditions: u'/U_{in} = 2% results in approximately 10% greater ignition delay than the case where u'/U_{in} = 0%. This effect of in-nozzle turbulence intensity on Spray D ignition delay is to be expected, given its effects on the physical spray characteristics in the inert cases and the dependence of ignition delay on mixing behavior.

Figure 8 compares the transient ignition process of Spray A (15.0% O_2, p_∞ = 6.00 MPa, T_∞ = 900 K, u'/U_{in} = 0%) and Spray D (20.9% O_2, p_∞ = 9.34 MPa, T_∞ = 900 K, u'/U_{in} = 2%) at various times normalized by LES ignition delay time $t^* = t/\tau_{ig}^{LES}$. At t^* = 0.85, formation of CH_2O can be seen at the core of both Spray A and Spray D, indicating the importance of low-temperature chemistry in the formation of CH_2O. Peaks of CH_2O are observed at the centers of both sprays, with concentration decreasing further downstream due to mixing with the ambient air. Subsequent formation of OH in both Spray A and Spray D can be
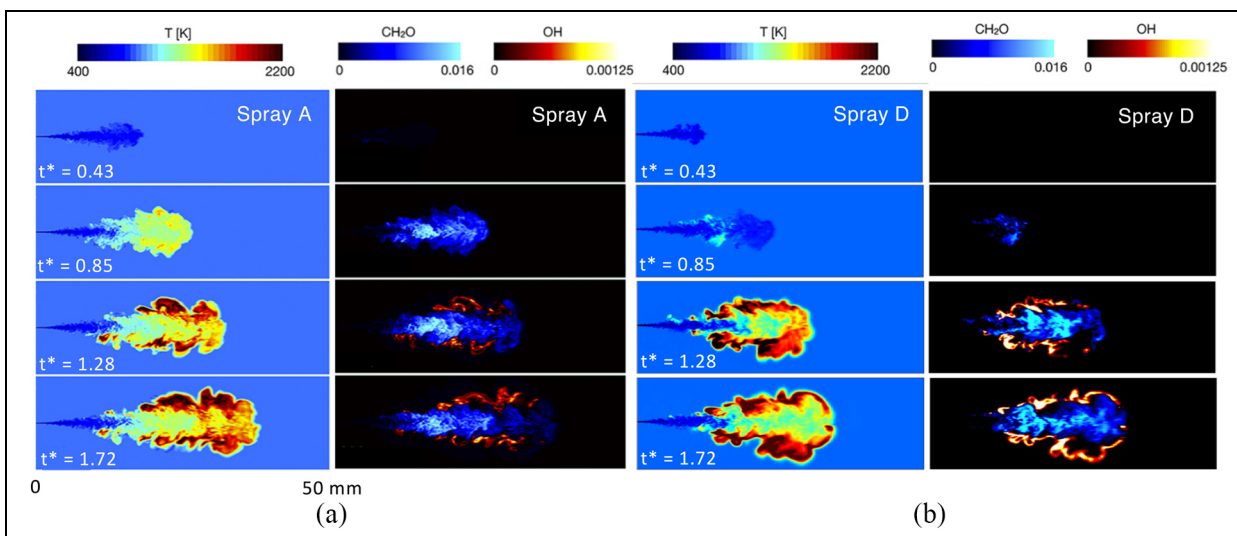
Figure 8. Comparison of transient temperature and intermediate species contours between (a) Spray A (15.0% O_2, p_∞ = 6.00 MPa, T_∞ = 900 K, u'/U_{in} = 0%) and (b) Spray D (20.9% O_2, p_∞ = 9.34 MPa, T_∞ = 900 K, u'/U_{in} = 2%) at various times normalized by LES ignition delay time, $t^* = t/\tau_{ig}^{LES}$.
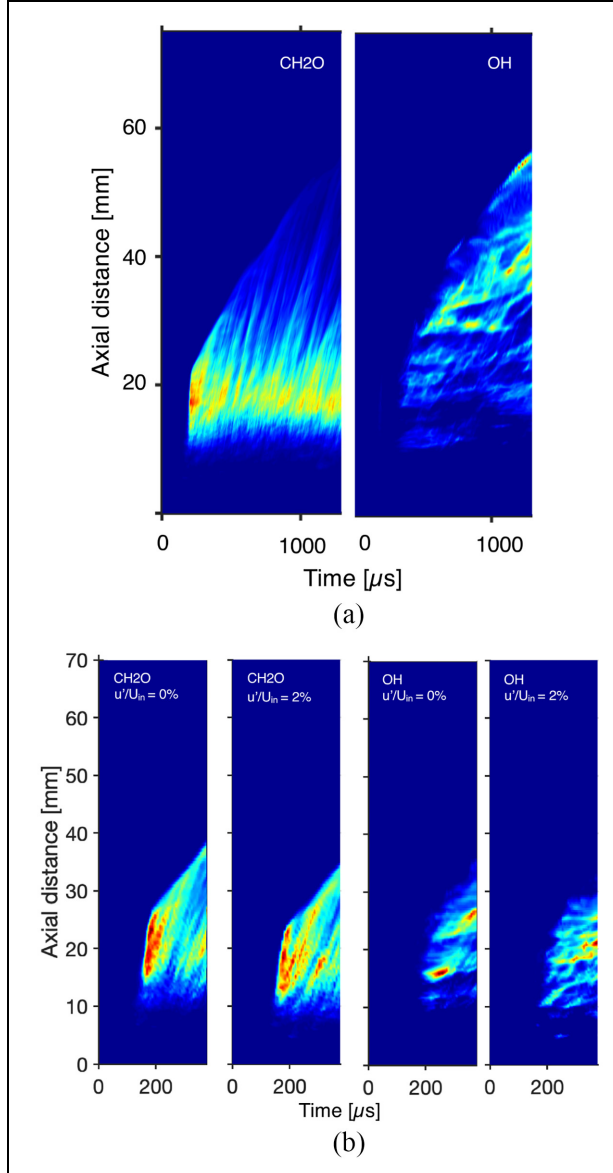
Figure 9. Comparison of I_{xt} plots for Spray A and Spray D; red denotes maximum intensity, while blue marks minimum intensity. (a) Spray A I_{xt} plots (15.0% O_2, $p_\infty = 6.00$ MPa, $T_\infty = 900$ K) with $u\bar{o}/U_{in} = 0$%. (b) Spray D I_{xt} plots (20.9% O_2, $p_\infty = 9.34$ MPa, $T_\infty = 900$ K) with $u'/U_{in} = 0$% and $u'/U_{in} = 2$%.

seen to occur with the consumption of CH_2O near the edges of the spray. Values of OH and CH_2O in the Spray D case are visibly higher, as caused by the higher ambient O_2 concentration.

The transient ignition behavior of Spray A and Spray D is further examined using the radially integrated intensity I_{xt} plots of OH and CH_2O—as employed by Maes et al.[18] I_{xt} for species i is defined by

$$I_{xt,i}(x,t) = \int \widetilde{Y}_i(x,y,t)\, dy \quad \text{with} \quad i = \{OH, CH_2O\}$$

(7)

In these plots, red denotes maximum intensity, while blue marks minimum intensity. In all cases presented,

CH_2O can be seen forming shortly before ignition. I_{xt,CH_2O} peaks before being consumed during OH production. Peaks of OH and CH_2O rarely coincide, with peak contours of OH present in the upper-right corners of the luminous region in all three plots, indicating that OH production occurs mostly far downstream from the nozzle. This is explained by the importance of low-temperature chemistry in the formation of CH_2O and high-temperature chemistry in the formation of OH.

The $I_{xt,OH}$ plot for Spray A presented in Figure 9(a) shows that the flame-lift off length, indicated by the slope on the bottom of the luminous region, stabilizes after $t = 1000$ μs. In Figure 9(b), note that the slope of the bottom border of the luminous region in the Spray D $I_{xt,OH}$ plots is still increasing. This indicates that the flame lift-off length has not stabilized for the simulation time presented. In Spray D, transient axial locations of both OH and CH_2O where $u'/U_{in} = 2$% are visibly shorter than the case where $u'/U_{in} = 0$%. Flame penetration, as indicated by the top border of the luminous region in the $I_{xt,OH}$ plot, is visibly 5 mm shorter in the case where $u'/U_{in} = 2$%. The sensitivity of Spray D to nozzle exit conditions is also seen to affect the reacting spray characteristics.

Conclusion

Large-eddy simulations of Spray A and Spray D have been performed using the diffuse-interface method and finite-rate chemistry, under inert and reacting conditions. Through parametric analysis, the sensitivity of spray breakup and ignition to in-nozzle turbulence is assessed.

With 0% turbulence intensity and a plug flow velocity profile at the inlet, inert Spray A vapor and liquid penetration predictions are found to be in good agreement with experimental data. At the same inlet conditions, Spray D liquid penetration predictions are in good agreement with experimental data, with a slight over-prediction seen for the vapor penetration length. Two parametric studies investigating the sensitivity of Spray D behavior to in-nozzle conditions have been performed—focusing on the effects of inlet velocity and on in-nozzle turbulence. Under identical mass-flow rates, the liquid and vapor penetration length of Spray D is found to be sensitive to the prescribed inlet velocity profile.

Increasing inlet turbulence intensity in Spray D is found to have a significant effect on the liquid and vapor penetration lengths. This is in contrast to Spray A where the vapor penetration length is found to be insensitive to turbulence at the inlet, whereas the liquid penetration length for Spray A decreases slightly under increasing turbulence intensity. A turbulence intensity of 2%, in conjunction with a plug flow inlet velocity profile, is found to provide the best agreement with Spray D experimental data.

In addition, simulations of Spray D reacting cases, at 0% and 2% inlet turbulence intensity, have been performed to investigate the effects of inlet turbulence on spray combustion behavior. Longer ignition delay is seen in the 2% case. Analysis of transient combustion behavior demonstrates decreased flame penetration and decreased lift-off length in the 2% case. A suitable treatment of Spray D in-nozzle phenomena is required for the accurate simulation of Spray D behavior under both inert and reacting conditions, the progress of which can be benefited by more experimental data.

Ignition delay in Spray A at 900 K ambient temperature and 6 MPa is under-predicted by a reasonable margin in comparison with experimental data. This discrepancy may be attributed to the simplified low-temperature oxidation sub-mechanism used in the finite-rate chemistry model. Ignition delay in Spray D at 900 K ambient temperature and 9.34 MPa is also under-predicted, but with a more significant error, with the additional error attributed to the higher ambient pressure. Spray D LES shows accurate ignition delay prediction at 6 MPa and 1200 K ambient pressure and temperature, where the low-temperature oxidation is less important.

Analysis of transient ignition behavior through radially integrated OH and CH_2O intensity plots of intermediate species shows qualitative matching behavior of intermediate species between Spray A and Spray D: the formation of intermediate species present during low- and high-temperature oxidation is captured.

These results and the analysis performed demonstrate that the LES method, employing finite-rate chemistry and a diffuse-interface formulation, is capable of capturing the complex behavior in transcritical diesel injection under different configurations, with especially accurate results at higher ambient temperature. The simulation results identify increasing sensitivity of upstream flow conditions with increasing nozzle turbulence, along with sensitivity to the inlet velocity profile. This indicates the need for quantitative velocity measurements to assess model accuracy.

Declaration of conflicting interests

The author(s) declared no potential conflicts of interest with respect to the research, authorship, and/or publication of this article.

ORCID iDs

Wai Tong Chung https://orcid.org/0000-0002-6447-4008

Matthias Ihme https://orcid.org/0000-0002-4158-7050

References

1. Engine Combustion Network, https://ecn.sandia.gov/
2. Lillo PM, Pickett LM, Persson H, Andersson O and Kook S. Diesel spray ignition detection and spatial/temporal correction. *SAE Int J Eng* 2012; 5(3): 1330–1346.
3. Skeen SA, Manin J and Pickett LM. Simultaneous formaldehyde PLIF and high-speed Schlieren imaging for ignition visualization in high-pressure spray flames. *P Combust Inst* 2015; 35(3): 3167–3174.
4. Crua C, Manin J and Pickett LM. On the transcritical mixing of fuels at diesel engine conditions. *Fuel* 2017; 208: 535–548.
5. Poursadegh F, Lacey JS, Brear MJ and Gordon RL. On the fuel spray transition to dense fluid mixing at reciprocating engine conditions. *Energ Fuel* 2017; 31(6): 6445–6454.
6. Poursadegh F, Lacey J, Brear M and Gordon R. The direct transition of fuel sprays to the dense-fluid mixing regime in the context of modern compression ignition engines. SAE technical paper 2018-01-0298, 2018, https://www.sae.org/content/2018-01-0298/
7. Falgout Z, Rahm M, Wang Z and Linne M. Evidence for supercritical mixing layers in the ECN Spray A. *P Combust Inst* 2015; 35(2): 1579–1586.
8. Malbec LM, Egúsquiza J, Bruneaux G and Meijer M. Characterization of a set of ECN Spray A injectors: nozzle to nozzle variations and effect on spray characteristics. *SAE Int J Eng* 2013; 6(3): 1642–1660.
9. Westlye FR, Battistoni M, Skeen SA, Manin J, Pickett LM and Ivarsson A. Penetration and combustion characterization of cavitating and non-cavitating fuel injectors under diesel engine conditions. SAE technical paper 2016-01-0860, 2016, http://papers.sae.org/2016-01-0860/
10. Gimeno J, Bracho G, Martí-Aldaraví P and Peraza JE. Experimental study of the injection conditions influence over n-dodecane and diesel sprays with two ECN single-hole nozzles. Part I: inert atmosphere. *Energ Conver Manage* 2016; 126: 1146–1156.
11. Payri R, Salvador F, Gimeno J and Peraza JE. Experimental study of the injection conditions influence over n-dodecane and diesel sprays with two ECN single-hole nozzles. Part II: reactive atmosphere. *Energ Conver Manage* 2016; 126: 1157–1167.
12. Payri R, Gimeno J, Cuisano J and Arco J. Hydraulic characterization of diesel engine single-hole injectors. *Fuel* 2016; 180: 357–366.
13. Martinez GL, Poursadegh F, Magnotti GM, Matusik KE, Duke DJ, Knox BW, et al. Measurement of Sauter mean diameter in diesel sprays using a scattering-absorption measurement ratio technique. *Int J Engine Res* 2019; 20(1): 6–17.
14. Magnotti GM and Genzale CL. Exploration of turbulent atomization mechanisms for diesel spray simulations. SAE technical paper 2017-01-0829, 2017, https://www.sae.org/content/2017-01-0829/
15. Magnotti G and Genzale C. Detailed assessment of diesel spray atomization models using visible and X-ray extinction measurements. *Int J Multiphas Flow* 2017; 97: 33–45.
16. Battistoni M, Magnotti GM, Genzale CL, Arienti M, Matusik KE, Duke DJ, et al. Experimental and computational investigation of subcritical near-nozzle spray

structure and primary atomization in the Engine Combustion Network Spray D. *SAE Int J Fuels Lubricant* 2018; 11(4): 337–352.

17. Matusik KE, Duke DJ, Kastengren AL, Sovis N, Swantek AB and Powell CF. High-resolution X-ray tomography of Engine Combustion Network diesel injectors. *Int J Engine Res* 2018; 19(9): 963–976.

18. Maes N, Meijer M, Dam N, Somers B, Toda HB, Bruneaux G, et al. Characterization of Spray A flame structure for parametric variations in ECN constant-volume vessels using chemiluminescence and laser-induced fluorescence. *Combust Flame* 2016; 174: 138–151.

19. Ma PC, Wu H, Jaravel T, Bravo L and Ihme M. Large-eddy simulations of transcritical injection and auto-ignition using diffuse-interface method and finite-rate chemistry. *P Combust Inst* 2019; 37(3): 3303–3310.

20. Ihme M, Ma PC and Bravo L. Large eddy simulations of diesel-fuel injection and auto-ignition at transcritical conditions. *Int J Engine Res* 2019; 20(1): 58–68.

21. Ma PC, Bravo L and Ihme M. Supercritical and transcritical real-fluid mixing in diesel engine applications. In: *Proceedings of the summer program*. Center for Turbulence Research, Stanford University, 2014, pp.99–108, https://web.stanford.edu/group/ctr/Summer/SP14/05_Two-phase_flows/06_ma.pdf

22. Matheis J and Hickel S. Multi-component vapor-liquid equilibrium model for LES of high-pressure fuel injection and application to ECN Spray A. *Int J Multiphas Flow* 2018; 99: 294–311.

23. Kaario OT, Vuorinen V, Kahila H, Im HK and Larmi M. The effect of fuel on high velocity evaporating fuel sprays: large-Eddy simulation of Spray A with various fuels. *Int J Engine Res*. Epub ahead of print 19 June 2019. DOI: 10.1177/1468087419854235.

24. Yue Z and Reitz RD. An equilibrium phase spray model for high-pressure fuel injection and engine combustion simulations. *Int J Engine Res* 2019; 20(2): 203–215.

25. Tsang CW, Kuo CW, Trujillo M and Rutland C. Evaluation and validation of large-eddy simulation sub-grid spray dispersion models using high-fidelity volume-of-fluid simulation data and engine combustion network experimental data. *Int J Engine Res* 2018; 20(6): 583–605.

26. Pei Y, Som S, Pomraning E, Senecal PK, Skeen SA, Manin J and Pickett LM. Large eddy simulation of a reacting spray flame with multiple realizations under compression ignition engine conditions. *Combust Flame* 2015; 162(12): 4442–4455.

27. Wehrfritz A, Kaario O, Vuorinen V and Somers B. Large eddy simulation of n-dodecane spray flames using Flamelet Generated Manifolds. *Combust Flame* 2016; 167: 113–131.

28. Kahila H, Wehrfritz A, Kaario O, Masouleh MG, Maes N, Somers B and Vuorinen V. Large-eddy simulation on the influence of injection pressure in reacting Spray A. *Combust Flame* 2018; 191: 142–159.

29. Pandurangi SS, Bolla M, Wright YM, Boulouchos K, Skeen SA, Manin J and Pickett LM. Onset and progression of soot in high-pressure n-dodecane sprays under diesel engine conditions. *Int J Engine Res* 2017; 18(5–6): 436–452.

30. Aubagnac-Karkar D, Michel JB, Colin O and Darabiha N. Combustion and soot modelling of a high-pressure and high-temperature dodecane spray. *Int J Engine Res* 2018; 19(4): 434–448.

31. Oefelein J, Lacaze G, Dahms R, Ruiz A and Misdariis A. Effects of real-fluid thermodynamics on high-pressure fuel injection processes. *SAE Int J Eng* 2014; 7(3), http://papers.sae.org/2014-01-1429/

32. Jahangirian S, Egelja A and Li H. A detailed computational analysis of cavitating and non-cavitating high pressure diesel injectors. SAE technical paper 2016-01-0873, 2016, https://www.sae.org/content/2016-01-0873/

33. Garcia-Oliver JM, Pastor JM, Pandal A, Trask N, Baldwin E and Schmidt DP. Diesel spray CFD simulations based on the—Eulerian atomization model. *Atomization spray* 2013; 23(1): 71–95.

34. Zhang W, Liu H, Liu C, Jia M and Xi X. Numerical analysis of jet breakup based on a modified compressible two-fluid-LES model. *Fuel* 2019; 254: 115608.

35. Ma PC, Lv Y and Ihme M. An entropy-stable hybrid scheme for simulations of transcritical real-fluid flows. *J Comput Phys* 2017; 340: 330–357.

36. Wu PK, Miranda RF and Faeth GM. Effects of initial flow conditions on primary breakup of nonturbulent and turbulent liquid jets. In: *32nd aerospace sciences meeting and exhibit (AIAA Paper 94-0561)*, Reno, NV, 10–13 January, 1994. Reston, VA: AIAA.

37. Poling BE, Prausnitz JM and O'Connell JP. *The properties of gases and liquids*. New York: McGraw-Hill, 2001.

38. Chung TH, Ajlan M, Lee LL and Starling KE. Generalized multiparameter correlation for nonpolar and polar fluid transport properties. *Ind Eng Chem Res* 1988; 27(4): 671–679.

39. Takahashi S. Preparation of a generalized chart for the diffusion coefficients of gases at high pressures. *J Chem Eng Jpn* 1975; 7(6): 417–420.

40. Yao T, Pei Y, Zhong BJ, Som S, Lu T and Luo KH. A compact skeletal mechanism for n-dodecane with optimized semi-global low-temperature chemistry for diesel engine simulations. *Fuel* 2017; 191: 339–349.

41. Goodwin DG, Speth RL, Moffat HK and Weber BW. Cantera: an object-oriented software toolkit for chemical kinetics, thermodynamics, and transport processes, 2018, https://www.cantera.org

42. Khalighi Y, Nichols JW, Lele SK and Ham Fand Moin P. Unstructured large eddy simulation for prediction of noise issued from turbulent jets in various configurations. In: *17th AIAA/CEAS aeroacoustics conference (32nd AIAA aeroacoustics conference, AIAA paper 2011-2886)*, Portland, OR, 5–8 June 2011. Reston, VA: AIAA.

43. Abgrall R and Karni S. Computations of compressible multifluids. *J Comput Phys* 2001; 169(2): 594–623.

44. Wu H, Ma PC and Ihme M. Efficient time-stepping techniques for simulating turbulent reactive flows with stiff chemistry. *Comput Phys Commun* 2019; 243: 81–96.

45. Tranquilli P and Sandu A. Rosenbrock-Krylov methods for large systems of differential equations. *SIAM J Sci Comput* 2014; 36(3): A1313–A1338.

46. Vreman AW. An eddy-viscosity subgrid-scale model for turbulent shear flow: algebraic theory and applications. *Phys Fluids* 2004; 16(10): 3670–3681.

47. Colin O, Ducros F, Veynante D and Poinsot T. A thickened flame model for large eddy simulations of turbulent premixed combustion. *Phys Fluids* 2000; 12(7): 1843–1863.

48. Wehrfritz A, Vuorinen V, Kaario O and Larmi M. Large Eddy Simulation of high-velocity fuel sprays: studying mesh resolution and breakup model effects for Spray A. *Atomization Spray* 2013; 23(5): 419–442.

49. Klein M, Sadiki A and Janicka J. A digital filter based generation of inflow data for spatially developing direct numerical or large eddy simulations. *J Comput Phys* 2003; 186(2): 652–665.

50. Segal C and Polikhov SA. Subcritical to supercritical mixing. *Phys Fluids* 2008; 20(5): 052101.